IDENTIFICATION OF FAILURE MECHANISMS IN THERMOPLASTIC COMPOSITES BY ACOUSTIC EMISSION MEASUREMENTS

M. G. R. Sause[1]*, J. Scharringhausen[2], S. Horn[1]
[1] Institute of Physics, University of Augsburg, Augsburg, Germany
[2] Composite Structures and Materials, MT-Aerospace AG, Augsburg, Germany
* Corresponding author (markus.sause@physik.uni-augsburg.de)

Keywords: *Fiber reinforced composites, Acoustic emission, Failure prediction, Finite element modeling*

1 Introduction

Fiber reinforced composite materials are a class of materials that show an extraordinary strength-to-weight and stiffness-to-weight ratio. However, the limited predictability of material failure requires a high margin of safety for the permissible design limits in construction of composite structures. Since global structural failure in composites is a consequence of a complex evolution of various microscopic failure mechanisms, to understand these evolution processes is key to understand global failure. Also, different failure mechanisms affect the structural integrity differently. Thus, it is essential to distinguish between different types of failure that occur within the structure under load.

While epoxy-based composites have been dominantly used in the past, the introduction of thermoplastic matrix materials introduces even more challenges for the prediction of failure. For the matrix material Polyphenylene sulfide (PPS) used in this study, the ratio of crystalline and amorphous regions depends on the thermal history of the material and can cause distinctly different interfacial properties [1]. Also, thermoplastic materials are sometimes applied at service temperatures above their glass transition temperature. This introduces pronounced non-linear degradation of their structural properties. In order to predict material failure of such structures under in-service conditions these effects have to be considered by respective failure theories.

To experimentally investigate evolution of damage in fiber reinforced composites a variety of methods can be applied. Imaging methods are frequently applied to visualize the damage progress after loading and unloading of test specimens. This allows monitoring of the damage progress in discrete steps only. Also, the unloading of the specimens causes existent cracks to close and makes them harder to detect. To overcome these problems the application of in-situ methods to detect active failure regions in the composite and to identify their time of occurrence is possible. However, continuous microscopy observation is either restricted to the specimen surface (optical microscopy or electron microscopy) or requires restrictions in specimen size or image resolution (X-ray tomography). Imaging methods, like digital image correlation (DIC), are used to spot damaged areas through sudden changes of the strain field. But in practice it is hard to distinguish between failure initiation and strain concentration at existing damaged areas. In the same way as hearing complements vision, acoustic emission (AE) can act complementary to imaging methods in order to improve detection of failure initiation.

One major source for AE in composites is the initiation and growth of damage. Microscopically this relates to the generation and propagation of cracks inside the matrix material, along the interface between matrix and fiber or the rupture of fiber filaments and combinations of these individual contributions. Another relevant AE source found in composites is friction between existing crack walls, which is frequently encountered when reloading damaged composites.

Consequently, in-situ measurement of acoustic emission signals during mechanical testing can assist to characterize specimen quality and to evaluate reliable failure criteria for composites. AE analysis can contribute in two ways to this task. Firstly by the determination of the AE source position during

loading of the specimen and, secondly, by the identification of particular failure mechanisms employing AE signal analysis.

While the method of AE source localization is already well established, identification of particular failure mechanisms is still a challenging task, but substantial progress has been achieved over the last two decades. To discuss this AE analysis method it is suitable to distinguish between the task of signal classification and the task of source identification. The first task involves the grouping of signals based on their similarity relative to each other. This is often achieved by analysis of signal features, i.e. parameters characterizing the detected signals. The methods to group AE signals range from simple approaches comprising discrete feature values to automated or semi-automated pattern recognition strategies. The second task is the assignment of one group of signals to a particular source mechanism. This is typically achieved by phenomenological approaches [2], by comparative measurement of specific test specimens producing known types of AE sources [3, 4] or microscopy investigations after loading [5]. Recent advances also allow the forward prediction of the emitted AE signal of a specific source type by analytical methods [6] or finite element modeling (FEM) [7, 8]. The latter allows direct correlation to microscopic failure mechanisms occurring in fiber reinforced composites.

In the subsequent section 2 we will outline the specimen preparation and the experimental configuration to obtain AE signals from tensile test at ambient temperature and at 160°C. Section 3 describes the FEM procedure of the AE sources that are observed in the experimentally used configuration. We introduce new aspects of the AE modeling concept featuring an improved AE source model. Section 4 presents the outcome of the experimental investigation and compares the experimental AE results to the FEM based AE results. Comparison of the localized AE source positions is made relative to positions of stress concentration obtained from DIC. We interpret the specimen failure in terms of the results obtained from our AE measurements as function of temperature. Section 5 is used to summarize the relevant findings for the thermoplastic fiber reinforced composites and how AE measurements can be used to interpret specimen failure beyond parameters from stress-strain curves.

2 Experimental

The specimens used in the present study are unidirectional fiber reinforced thermoplastic composites made from Torayca T700S 12k carbon fibers and PPS matrix material. Two different production processes were investigated. One type of specimens was manufactured by heat pressing using a thermal treatment cycle with 15 minutes hold time at 320 °C and heat and cooling rates of 5 to 15 °C/min. The other type of specimens was built by in-situ laser consolidation of thermoplastic tapes.

All specimens were cut to nominal specimen dimensions of 250 mm × 15 mm × 1 mm (length × width × thickness) with the fiber axis direction parallel to the length direction of the specimen. Since thermal treatment of the specimens subsequent to the production process can influence the measured material properties, the room temperature curing adhesive system Stycast 2850 FT was used to bond specimens and reinforcement tabs with (± 45° layup) to the heat pressed specimens. For the specimens manufactured by in-situ laser consolidation, integral reinforcements in form of inserted ± 45° plies were fabricated, that increase the nominal thickness in the gripping area to 1.5 mm. These integral reinforcements were found to be superior to conventional adhesive bonding of reinforcement tabs, since they completely prevent AE signals that may occur due to failure of the adhesive bonding.

The heat pressed specimens were tested in displacement controlled mode with 2 mm/min test speed using an universal testing machine with 250 kN load cell and hydraulic grips. The in-situ consolidated specimens were tested inside a temperature chamber at ambient temperature conditions and at 160°C using wedge grips under otherwise identical conditions. For all configurations, strain measurements with initial gage length of nominally 70 mm were carried out on the specimen using the digital image correlation mode of an optical extensometer of type “VideoXtens”.

Also, for all configurations, AE sensors were mounted on the specimen using suitable clamp systems to ensure reproducible contact pressure between sensor and specimen. As acoustic couplant, viscous Baysilone silicone grease was used. The temperature stability of the couplant has been tested previously by thermal cycling in face-to-face arrangement with mutual pulsing of the sensors. The

average loss of sensitivity was 12 dB at 160 °C compared to the ambient temperature conditions. Although the selected couplant degrades significantly at 160 °C, the absolute sensitivity was found to be superior to five other couplants evaluated using the same approach.
The AE signals were detected using two type WD multi-resonant sensors in linear arrangement and a PCI-2 data acquisition card. All signals were amplified by 20 dB using a 2/4/6 preamplifier and recorded with 35 dB threshold and 10/80/300 settings for Peak-Definition-Time/Hit-Definition-Time/Hit-Lockout-Time using the software AEwin with 10 MHz sampling rate. For all configurations, a bandpass filter from 20 kHz to 1 MHz was used. To detect only AE signals with source positions located in the tapered area, an Event-Definition-Time filter was used. The settings for this filter were adjusted for each specimen individually. Using pencil lead breaks on the grips, in front and behind the sensor, the length of the Event-Definition-Time was suitably selected.
DIC-measurements were carried out for specimens at room temperature using an ARAMIS 12M system synchronized to the universal testing machine and the AE system. Images were detected in 2D mode with 2 Hz acquisition rate and polarizing filters. The field of view was on the opposite side of the optical extensometer on the planar side of the specimen.
In total, 17 specimens were tested at 23 °C (ambient temperature) and 6 specimens at 160 °C (elevated temperature) conditions.

3 FEM modeling of AE sources

In order to assign the detected AE signals to a particular mechanism, a method of validation is required. The FEM modeling of AE signals described in the following is based on various previous publications. Therefore, the major findings are briefly summarized and only new contributions to this field are presented in the following sub-sections.
There are three aspects to modeling of AE. The first aspect is the modeling of the AE source generating the AE signal. In analytical approaches and early FEM work the AE sources are represented by point source models [9, 10]. While such models already yield valuable insights to the relation between source position and excited wave types [10], their geometrical complexity is not sufficient to represent failure in composite materials. To overcome this problem an AE source model was introduced, that takes into account the geometrical arrangement of fibers and distinguishes between the elastic properties of fiber and matrix material [8, 11]. From this model it was concluded that even for identical source position, different failure mechanisms will yield distinctly different AE signals, which can be distinguished by their frequency content.
After the excitation process, the next important aspect in modeling of AE is the description of wave propagation in an appropriate geometrical configuration. For the case of fiber reinforced materials, the individual ply orientations and the presence of edges have to be taken into account. Since modeling of guided ultrasonic waves is considered to be well established, only aspects relevant for AE testing were investigated in detail. This includes the influence of specimen geometry [12] and the influence of internal discontinuities and damage within the propagation path of the AE signal [13].
The detection process of the AE signal by a particular AE sensor type is the last step missing to complete the full chain of modeling work. The resonance characteristics of many commercial sensors can significantly alter the detected frequency spectra [12]. Therefore, their frequency dependent detection sensitivity has to be taken into account to allow for a comparison between experimental and modeled AE signals. Beyond the valuable approaches of forward modeling [6], we recently developed a comprehensive FEM based approach for modeling of AE sensors that incooperates the piezoelectric conversion and the influence of the attached circuitry [14].
The model configuration used for the present investigation is depicted in figure 1. It consists of a macroscopic 3D model including the full specimen geometry and a model of the type WD piezoelectric sensor. Embedded within the macroscopic model is a cubical representative volume element (RVE) with 100 µm edge length including a spherical transition region acting as perfectly matched layer (PML). Within the RVE various failure mechanisms are modeled as will be described in subsection 3.1. The source is positioned at different locations within the macroscopic specimen to obtain signals for a variety of source-sensor distances. Within the software

environment COMSOL we chose the global mesh resolution to be 1 mm with local refinement down to 1 µm in the RVE domains using quadratic order elements. The time-step used was 5×10^{-8} s. Both settings were validated to achieve convergent results in previous investigations [8, 11-14].

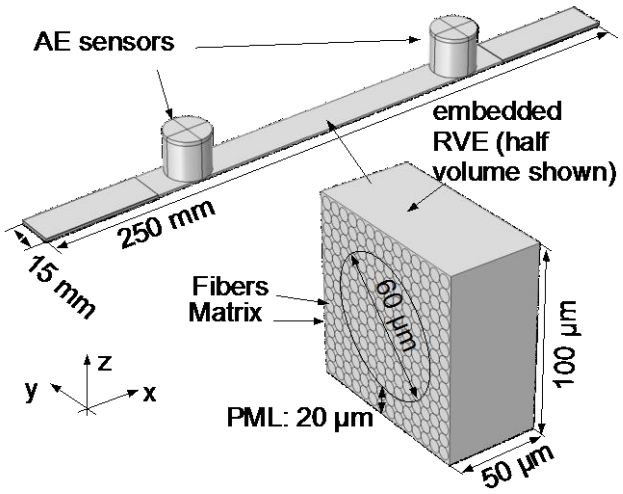

Fig.1. Multiscale model used for finite element modeling of acoustic emission signals.

3.1 FEM modeling of AE source types

In order to model AE signals originating from a failure mechanism in fiber reinforced materials, a micromechanical representation of the crack geometry is modeled within the RVE. To excite an AE signal, the crack surface is deflected by a force vector F_t with magnitude F_e within a specific source rise-time t_e. The displacement function is defined as step-function type with cosine-bell shape:

$$F_t = \begin{cases} 0 & t < 0 \\ F_e\left(0.5 - 0.5\cos\left(\frac{\pi t}{t_e}\right)\right) & 0 \le t \le t_e \\ 0 & t > t_e \end{cases} \quad (1)$$

Suitable assumptions have to be made for the force magnitudes, their direction and the rise-time of the source. The force magnitudes are based on the comparison of the modeled and the experimental signals magnitude. The direction of the force excitation is given by the modeled mode of fracture. The rise-time is an estimate, but has been validated in its order of magnitude and is expected to be correlated to the type of fracture [8, 11].

To achieve the transition between the inhomogeneous material properties on the microscopic scale and the homogeneous material properties on the macroscopic scale, we use a PML approach. In the current model we define pure material properties $C_{ij,0}$ (i.e. fiber and matrix) in the inner spherical volume with radius r_{pure} = 30 µm. Within the PML sphere with radius r_{pml} = 50 µm we gradually change the elastic properties using intermediate properties C'_{ij} as function of radial position r (with r = 0 at the center of the RVE cube). The material properties used are given in table 1. The intermediate properties C'_{ij} are defined as:

$$C'_{ij} = C_{ij,0} + \left(\left(\frac{r}{r_{pure}} - 1\right) \cdot \left(C_{ij,1} - C_{ij,0}\right)\right) \quad (2)$$

$$r_{pure} \le r \le r_{pml}$$

On the macroscopic scale (outside the RVE region) the composite properties are modeled as anisotropic continuum $C_{ij,1}$. Before fracture occurs, materials deform with substantial contributions of plastic deformation. Also, polymers materials can exhibit significant contributions of viscoelastic material response. The current model neglects these contributions, since the AE release (i.e. generation of elastic waves) is dominated by the elastic material response. Therefore, the proposed model should not be understood to model crack propagation from a fracture mechanics point of view, but to test different configurations and predict their influence on AE release.

Material	**Density [kg/m³]**	**Poisson's ratio [1]**	**Modulus [GPa]**
T700S fiber	1800	0.20	230.0
PPS	1350	0.36	3.8
Composite	1600	-	C_{11} = 152.7
			C_{12} = 4.7
			C_{23} = 4.4
			C_{22} = 11.7
			C_{44} = 4.5

Tab.1. Elastic properties used for FEM.

For the unidirectional tensile test investigated, only few micromechanical failure types are likely to occur. Following the categorization of numerous failure theories (see [15] for an overview) we

distinguish between fiber failure (FF) and failure between the fibers, referred to as matrix failure or inter-fiber failure (IFF). As additional AE source type, we present the configurations used to model different types of interfacial failure, namely fiber-matrix debonding and delamination failure (DEF).

3.1.1 Fiber failure (FF)

The geometrical configuration used to model fiber failure is shown in figure 2. To simulate single fiber failure, one fiber within the RVE is splitted and the source function (1) is applied to the newly formed edges of the fiber acting in opposite directions. This is indicated by the arrows in figure 2. Force magnitude was chosen to result in 2 µm residual fiber displacements based on the values reported by Scott et al. [16]. The source rise-time was chosen to be $t_e = 5 \times 10^{-8}$ s based on the findings of our previous publication [8].

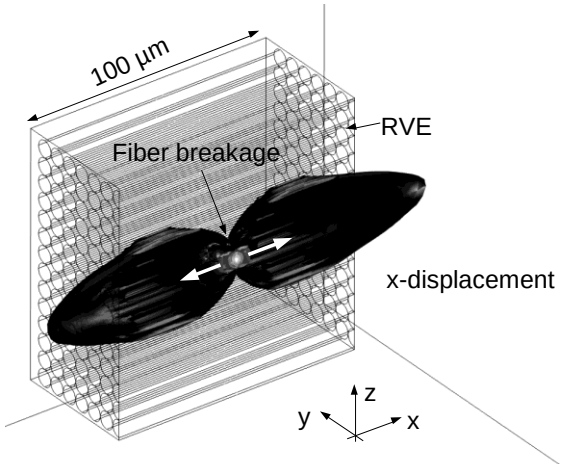

Fig.2. x-displacement field of fiber failure model at $t = 5 \times 10^{-8}$ s. Source excitation direction is marked by arrow, volume shown is symmetric at xz-plane.

To simulate failure of a fiber bundle, the configuration of figure 2 was modified to allow simultaneous displacement of 13 fibers and the interjacent matrix region. The latter is justified by the assumption, that the matrix material surrounding the breaking fibers cannot withstand the local energy release and will break together with the fiber filaments. In both cases, the displacement field obtained at $t = 5 \times 10^{-8}$ s after source excitation resembles a dipole characteristic with dipole axis aligned parallel to the fiber axis.

3.1.2 Inter-fiber failure (IFF)

Due to the variety of potential fault planes, the geometrical configuration to model IFF is more complex than for FF. Three of the eight geometrical source configurations tested are shown in figure 3-a and 3-b.

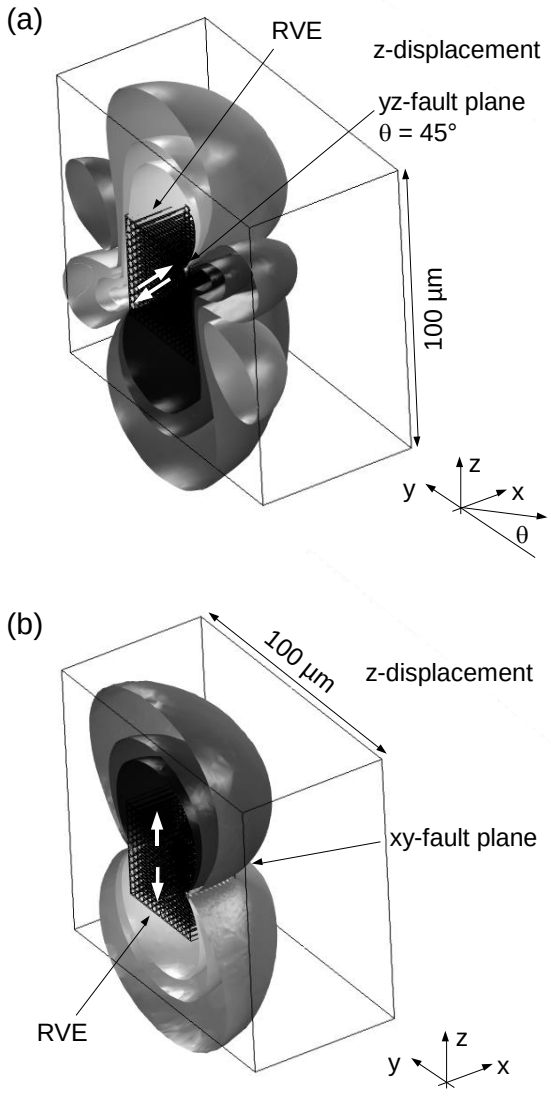

Fig.3. z-displacement fields of inter-fiber failure models at $t = 5 \times 10^{-8}$ s. Failure modes considered are of in-plane shear type (a) and out-of-plane type (b). The respective source excitation directions are marked by arrows, volume shown is symmetric at yz-plane.

The mode of failure considered in figure 3-a is of the in-plane shear type (mode-II). The movement of the fault planes is in opposite direction relative to each

other, as indicated by the arrows. The orientation of the fault plane was varied between θ = 0° to θ = 90°. Figure 3-a shows the displacement field obtained at $t = 5 \times 10^{-8}$ s after source excitation of the configuration with θ = 45°. For all configurations, the displacement field is described best as quadrupole characteristic.

Based on established failure theories one would not expect more than the Mode-II dominated failure type for the macroscopic loading condition given. However, due to the inhomogeneous microstructure of the material and existing damage zones, other loading conditions may also exist on the microscopic scale. Therefore we modeled the out-of-plane (mode-I) condition with angles θ = 0° and θ = 90° as shown exemplarily in figure 3-c for θ = 0° as potential AE source. For these configurations the displacement field resembles a characteristic dipole pattern with dipole axis parallel to the fault plane normal.

For all IFF configurations we chose the force magnitude $F_e = 0.5$ N and the source rise-time to be $t_e = 1$ µs.

3.1.3 Fiber-matrix debonding and delamination failure (DEF)

Beyond the failure mechanisms FF and IFF, we consider the process of fiber-matrix debonding and inter-ply delamination as potential AE sources. Typically both failure mechanisms are included as IFF types in the respective failure theories [17]. But from the AE point of view some fundamental differences exist, which distinguish the DEF source configurations from the IFF configurations as described in subsection 3.1.2. As indicated by the arrows in figure 4, for the case of inter-ply delamination, various fault plane movements are expected.

Assuming the fibers are under compressive or tensile thermal stress states before failure, the sudden removal of bonding between fiber and matrix is likely to cause short relaxation of the fiber filament. This will cause a short displacement oriented along the fiber axis direction. Since in the present AE source model, we assume, that the fiber does not break, only force magnitudes $F_e = 0.05$ N much smaller than those for the FF model were considered. Due to the partial or complete debonding between fiber and matrix, a displacement component normal to the fault plane is expected. The choice for force magnitudes in this direction follows the considerations for IFF. As source rise-times, we use $t_e = 0.1$ µs for the direction along the fiber axis and $t_e = 1$ µs for the direction normal to the fault plane. The displacement field obtained after $t = 5 \times 10^{-8}$ s is shown in figure 4-a for the z-displacement and in figure 4-b for the x-displacement, respectively.

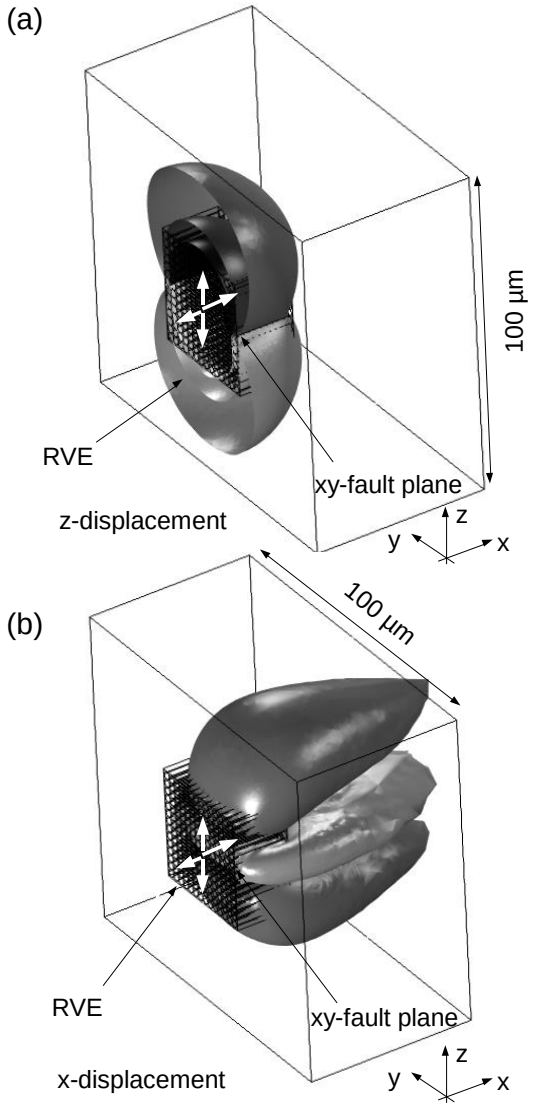

Fig.4. Displacement fields of inter-ply delamination model in z-direction (a) and x-direction (b) at $t = 5 \times 10^{-8}$ s. The respective source excitation directions are marked by arrows, volume shown is symmetric at yz-plane.

Due to the different excitation conditions, the radiation pattern consists of one dipole contribution with axis parallel to the z-axis and a quadrupole field with radiation pattern in the xz-plane. Due to the simultaneous excitation of 12 fibers, the quadrupole is elongated along the y-axis.
The main differences to the AE source model for fiber-matrix debonding is geometrical arrangement of the fault plane. For debonding of a single fiber, one force component is acting along the fiber axis direction. Due to the debonding, a second component is defined acting in the θ-direction. Due to variations in the microstructure and the local neighborhood, this component does not necessarily have equal displacement magnitude to all θ-directions, which was considered by simulation runs with asymmetric force distributions with respect to θ. The choice of displacement magnitudes and source rise-times follows the same considerations as made for inter-ply delamination.
Due to the increased number of free parameters of the DEF models, we conducted multiple runs comprising different ratios between forces parallel and perpendicular to the fiber axis direction. By definition, a negligible displacement magnitude in fiber axis direction will yield a pure IFF model and a negligible displacement magnitude in θ-direction will yield a pure FF model, respectively. Therefore, from the AE point of view, the DEF source configuration may be understood as intermediate configuration of both cases.

3.2 Variation of AE source position

As described in the previous subsection, the different AE source models allow simulation of various failure types in fiber reinforced composites. Consistent to the reports of previous publications [8, 11, 12], the different AE source configurations cause excitation of distinctly different AE signals within the modeled geometry. The difference in the frequency spectra of the detected AE signals modeled for FF, IFF and DEF is the basis to distinguish different types of failure in composites by AE analysis.
For the present plate-like geometry the excited waves are Lamb-waves with symmetric or antisymmetric motion relative to the medial plane of the plate. Due to the thin thickness (1 mm) only the fundamental modes are observed in the experimentally used frequency range.
Since AE source positions are found distributed within the tapered region of the specimen, it is not suitable to consider only one (xy)-coordinate as AE source position. As pointed out by Hamstad et al. [10], the z-position of the AE source within the plate is crucial for the excitation ratio of symmetric and antisymmetric Lamb-wave modes. Therefore we systematically vary the position of the AE source along the x-, y- and z-axis to span the full volume investigated experimentally.
At the designated AE sensor positions (see figure 1), the calculated surface displacement is converted into a voltage signal using simulation of piezoelectric conversion using a model of the WD sensor type. A full description of the sensor modeling procedure is given in [14] with details of the material parameters used in [12]. Taking into account the sensor characteristic, it is possible to compare the simulated voltage signals directly to experimental signals.
For AE sources being larger in dimension than those proposed by the presented AE source model, a superposition of the various microscopic failure types can be expected.
In total 72 simulation runs were carried out to obtain 144 modeled AE signals with different failure types for comparison to experimental AE signals.

4 Results and Discussion

For all specimens, the failure strength and the tensile modulus was calculated from the stress-strain curves. All AE signals were subject to the conventional Δt localization routine to obtain the x-coordinate of the AE source position. Subsequently, the features listed in table 2 were calculated from the first 100 µs after threshold crossing. The unsupervised pattern recognition approach to detect mathematically meaningful partitions of AE signals by analysis of the extracted feature values is comprehensively described in [18]. For the present investigation we investigated all permutations of the features listed in table 2 with subset sizes ranging from five to ten. The features evaluated are extracted from the first 100 µs after threshold crossing of the AE signals in time domain $U(t)$ and from their FFT $\widetilde{U}(f)$, respectively. A detailed description of the features is found in references [12, 18].
Similar to the procedure described in [19] we used a two-stage approach, which yields three

distinguishable types of AE signals for each specimen tested at ambient temperature and at 160 °C.

AE feature	Definition
Average Frequency [kHz]	$\langle f \rangle = N_{AE}/t_{AE}$
Reverberation Frequency [kHz]	$f_{rev} = \frac{N_{AE} - N_{peak}}{t_{AE} - t_{peak}}$
Initiation Frequency [kHz]	$f_{init} = N_{peak}/t_{peak}$
Peak-Frequency [kHz]	f_{peak}
Frequency centroid [kHz]	$f_{centroid} = \frac{\int f \cdot \widetilde{U}(f)df}{\int \widetilde{U}(f)df}$
Weighted Peak-Frequency [kHz]	$\langle f_{peak} \rangle = \sqrt{f_{peak} \cdot f_{centroid}}$
Partial Powers [%]	$\frac{\int_{f1}^{f2} \widetilde{U}^2(f)df}{\int_{0kHz}^{1200kHz} \widetilde{U}^2(f)df}$
Partial Power 1 [%]	f_1 = 0 kHz; f_2 = 150 kHz
Partial Power 2 [%]	f_1 = 150 kHz; f_2 = 300 kHz
Partial Power 3 [%]	f_1 = 300 kHz; f_2 = 450 kHz
Partial Power 4 [%]	f_1 = 450 kHz; f_2 = 1200 kHz

Tab. 2. Extracted AE signal features used for the pattern recognition approach.

It is worth noting that due to the changed elastic properties at elevated temperatures a shift of the mean frequency spectra is observed. This causes distinctly different features being picked by the pattern recognition algorithm for clustering of the AE signals detected at ambient temperature and those detected at 160 °C. For ambient temperature conditions, the features "Peak-Frequency", "Weighted Peak-Frequency", "Partial Power 2", "Partial Power 3" and "Partial Power 4" were selected. For the tests at 160 °C, the feature combination "Peak-Frequency", "Weighted Peak-Frequency", "Reverberation Frequency", "Partial Power 1" and "Partial Power 2" were found to yield the best partition.

4.1 Comparison to FEM-prediction

The partition of AE signals obtained by unsupervised pattern recognition is shown in figure 5-a for one representative specimen of the measurements under ambient conditions. To visualize the separation of the signal clusters, a projection to the feature axis Weighted Peak-Frequency and Partial Power 2 was used. For the experimental data, the clusters are well defined, but their edges are close together. As recently discussed [20] this may cause an uncertainty in the assignment of the signals to a respective cluster.

For the simulated AE signals, the same feature values are extracted and are plotted in figure 5-b.

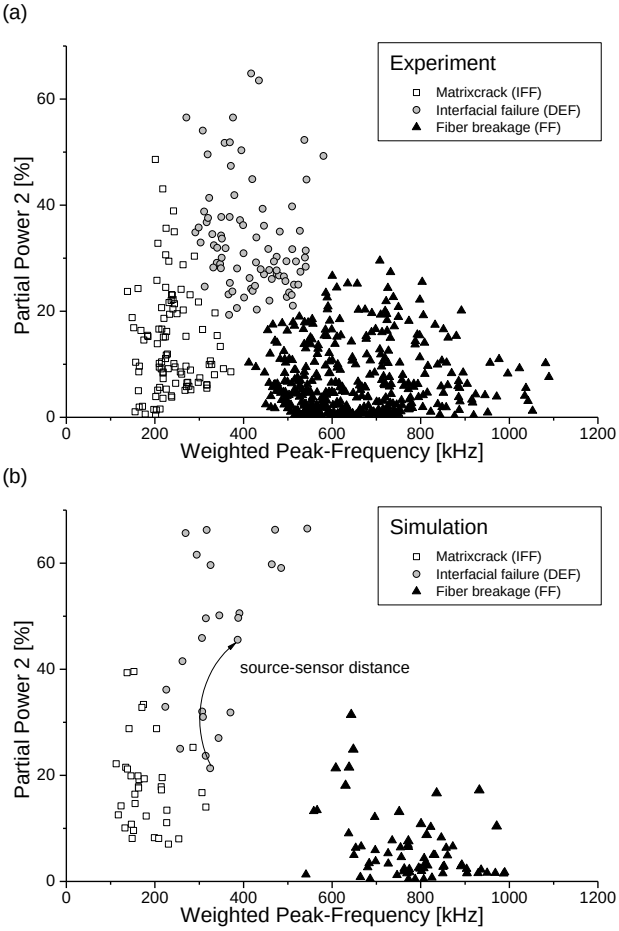

Fig.5. Comparison between feature values extracted from experimental (a) and simulated (b) AE signals.

The signals simulated for fiber failure and fiber bundle failure are well separated from the rest of the signals. Compared to the experimental data, the simulated signals show slightly higher frequency contributions. One possible explanation for this discrepancy is the influence of strong attenuation effects for higher frequencies in thermoplastic composites. For the previous investigations on epoxy-based composites no such influence was observed.

The feature values extracted from simulated signals for matrix cracking and interfacial failure are observed within similar ranges as for the

experimental data. Signals originating from inter-fiber failure in Mode I condition are found with lowest “Partial Power 2”. The simulations of inter-fiber failure under Mode II conditions are found with higher “Partial Power 2” values up to 40 %. The variation of the θ-direction of the fault plane causes variability in the absolute values as seen in figure 5.b, but does not substantially change the extracted feature values. This behavior is unexpected, since the geometrical arrangement was rotated by 90°. As described in subsection 3.1, this causes distinctly different source radiation patterns. Therefore, we conclude, that the microstructure (e.g. fault plane roughness) and the rise-time is the dominating factor for this source type.

For inter-ply delamination a small overlap to the feature value ranges of matrix cracking is found. This is in very good agreement to the experimental observations. However, the separation to signals associated with fiber breakage is much more pronounced in the simulation data than in the experimental data. One possible explanation is a larger variability in the experiment than currently considered in the AE source models. Another possibility is the existence of other distinct source configurations considered as interfacial failure, which were not modeled so far.

For all AE source configurations, the variation in distance between AE source and AE sensor causes the overall extent of the clusters as seen in figure 5-b. As example, the feature trajectory for a change in source-sensor distance is marked for one case of inter-ply delamination.

Based on these findings it is possible to conclude, that the clusters detected by the pattern recognition approach allow meaningful distinction between the occurrence of fiber breakage (FF), matrix cracking (IFF) and interfacial failure (DEL) as described in subsection 3.1.

Beyond the nature of the AE source, other factors are known to affect the position and overlap of the clusters associated with a particular failure mechanism. In addition to the source-sensor distance mentioned above, the signal-to-noise ratio, the ply layup, complex 3D-geometries of the individual plies (e.g. fabrics) and the AE sensor type will affect the quality of the partition. In the worst case, the sum of the negative effects will cause significant overlap of the clusters. For such cases, any attempts to distinguish AE signals using unsupervised pattern recognition strategies are unlikely to yield meaningful partitions of clusters.

4.2 Comparison to DIC

In the following we present a comparison between DIC measurements and AE source localization results. There are two major drawbacks of the DIC systems for assessment of failure locations in composites. First, despite of high-resolution camera systems, the spatial resolution of DIC systems is still limited and strain concentration at distinct positions is not necessarily identical to initiation or growth of damage. Second, at higher load levels, the spray pattern may easily drop down as consequence of preliminary rupture of some fiber filaments. For both drawbacks, AE comprises an ideal complementary method as described in the following.

The DIC results in figure 6 show the x-strain field at the initial state and after specimen loading of t = 45 s for one representative specimen. The AE source positions localized for the specimen are shown for the same x-scale as the DIC results. As plotted on the vertical axis, the AE sources are observed at distinct load levels and can be correlated to all but two of the signatures of the x-strain field of the DIC measurements. One possible explanation for these DIC signatures without associated AE signals is a substantial strain concentration before failure initiation. Another possibility is the missing detection of the associated AE signal.

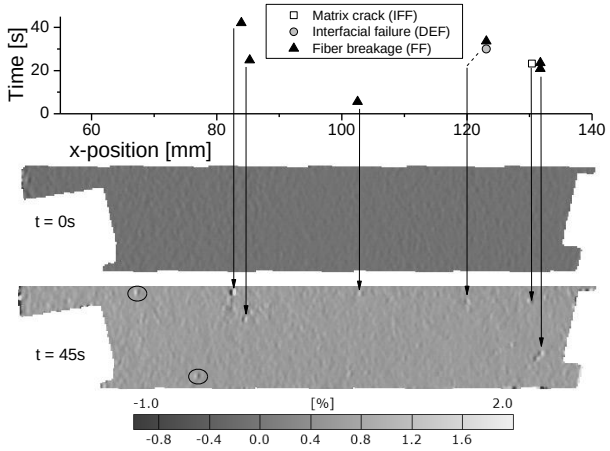

Fig.6. Comparison between DIC measurement and localized AE source positions.

As seen from figure 6, AE complements the DIC measurement by adding information regarding the

failure mechanism as indicated by the different symbols. Also, the presence of an AE source close to the position of strain increase can act as strong indicator for failure initiation, or failure growth at this location. Superior to AE source localization accuracy, DIC measurements provide significantly better spatial representations of failure locations and allow easy tracking of their growth.

However, due to the large number of AE signals detected during a single experiment, a manual correlation of AE source positions to imaging methods as in figure 6 is more than burdensome. To effectively combine both methods, an automated routine was developed within the software package ImageJ to combine images of the DIC analysis software GOMInspect and the AE source visualization package DensityVille. This allows simultaneous tracking of results from both methods in one image series and yields a powerful combination of both experimental techniques.

4.3 Relation between AE results and mechanical properties

Following reference [21], we quantified the average amplitude per AE signals for the individual failure mechanisms. As shown in figure 7, these show distinct correlation to the failure strength of the specimens measured at ambient temperature (figure 7-a). The investigated heat-pressed specimens were all found to have higher failure stress values than the in-situ consolidated. For every mechanism, a decrease in average signal amplitude was found with increasing failure strength. Although this behavior is counter-intuitive, it is expected for tensile testing of unidirectional specimens. Based on the generalized theory of AE [9] an intrinsic relation between the AE amplitude and the size of the damage zone is expected. If failure inside the specimen is due to localized single events, the specimen is severely damaged at this position and cannot withstand the increasing load level for a long time. If failure is due to multiple events with minor damage, the surrounding regions can compensate the damaged area and the specimen will withstand the load for a longer time. Interesting differences between in-situ consolidated specimens and heat-pressed specimens were found for the average amplitude per signal of matrix cracking. The average amplitudes are significantly higher for the heat-pressed specimens. This indicates that inter-fiber failure in these specimens occurs in larger steps, than for the in-situ consolidated specimens. An analysis of the video observations recorded during testing confirms this conclusion. Preliminary filament failure at the specimen edges is assumed to induce further inter-fiber failure under continuous loading. This was observed significantly less for the heat-pressed specimens.

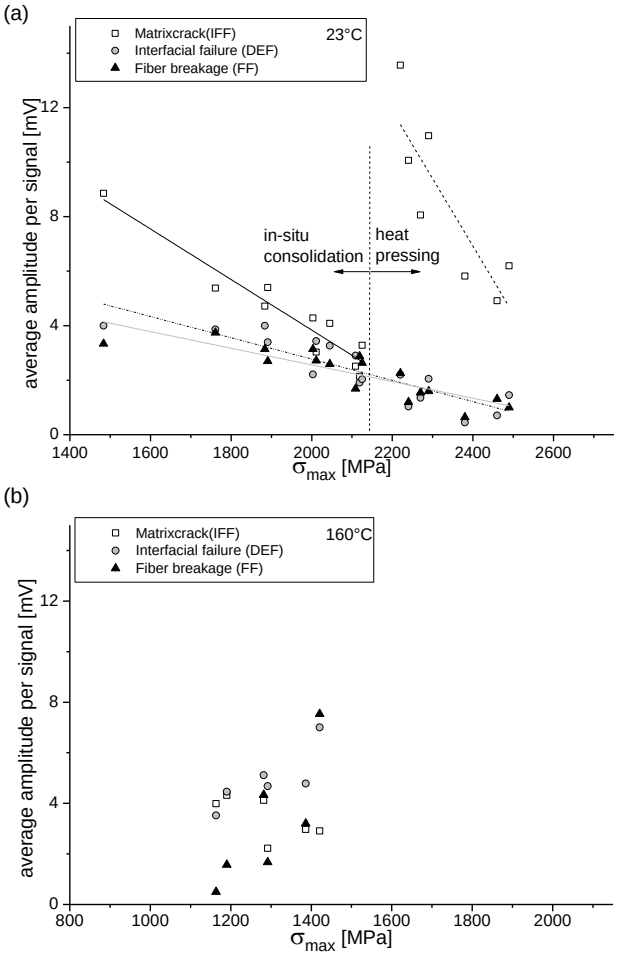

Fig.7. Average amplitude per signal quantified for the different failure mechanisms for measurements at 23 °C (a) and at 160 °C (b) temperature.

For the in-situ consolidated specimens measured at 160 °C distinctly different behavior is observed. Due to the elevated temperature conditions, the failure strength is much less and the failure mode is more ductile than for the ambient temperature specimens. This causes much less AE signals, i.e. only 6 to 17 for fiber breakage signals. Therefore, the calculated average signal amplitude is significantly influenced by the high amplitude of the final failure signals.

Therefore, the inverse trend of the average signal amplitudes of fiber breakage and interfacial failure with failure strength seen in figure 7-b should be interpreted with care. Within the standard deviation of the signals contributing to the respective clusters, no significant trend is seen in figure 7-b.

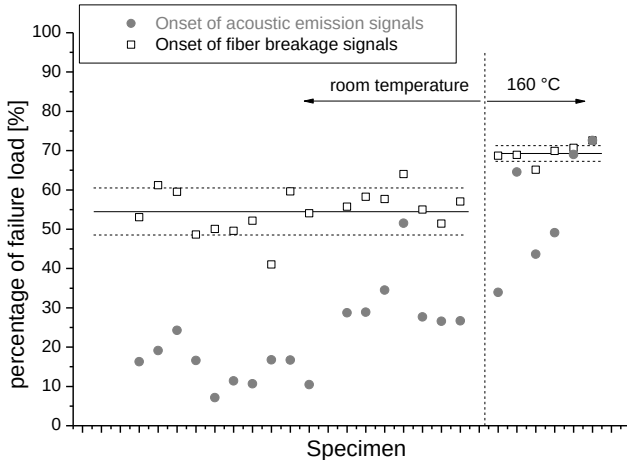

Fig.8. Acoustic emission onset of fiber breakage signals compared to onset of all signals.

Relevant for conformation of failure theories and failure prediction and is the experimental detection of initiation of specific failure modes. To demonstrate the usage of AE in this context, we measure the global AE onset and the AE onset for fiber breakage signals. The ratio of the load level at AE onset and the failure load is shown in figure 8. The average onset of FF signals is quantified to be at around 54 % of the failure load for ambient temperature tests and around 69 % for 160 °C temperature tests. In comparison, the overall onset of AE signals is subject to large scattering and is found at fairly lower load levels. The associated signals originate from IFF and DEF and can be correlated to the initiation of damage occurring at the side surface of the specimens and distinct positions within the specimen. For the tests at 160 °C temperature, a shift in failure onsets to larger loads is observed. This is caused by the substantially reduced brittleness of the PPS at elevated temperatures.

These findings are strong indicators, that meaningful identification of failure modes in thermoplastic composites is possible by AE analysis.

5 Conclusion

The improved geometrical representation of the AE source model allows an investigation of a broad range of failure mechanisms that occur in fiber reinforced composites. The present work demonstrates the applicability of this model based AE analysis in combination with DIC to assist in the interpretation of tensile specimen quality. The fiber reinforced thermoplastic composite specimens used in this study were fabricated by heat-pressing and in-situ laser consolidation. For both specimen types, distinct differences in their AE activity and their failure strength were observed. The quantified relative amplitude of AE signals shows strong correlation to the measured failure strength of the specimens.

The identification of the onset of fiber failure comprises a better quantity to predict structural failure than the overall onset of AE signals. This is due to the fact, that the fibers are the load bearing part and their failure initiates the ultimate failure of the composite. Due to the change in brittleness of the thermoplastic PPS matrix, different behavior is observed at ambient temperature conditions and at elevated temperature for both, AE signal activity and the mechanical properties of the specimens.

These findings are strong indicators that meaningful identification of failure modes by AE analysis is a key to improve our understanding of composite failure. In particular, the combination of in-situ methods like DIC and AE can assist to improve the predictive capabilities of current composite failure theories, e.g. for superimposed stress-states. Onsets of specific AE signals and their felicity ratios can be used to assess specimen quality under cyclic loading conditions [19].

The valid identification of failure modes is also a key to allow meaningful online monitoring of composite structures by AE analysis. In such environments, AE signals are expected to also originate from a variety of noise sources. Associated modeling work can aid in the task to distinguish such AE noise sources from AE signals due to actual damage. Therefore, the next step is the consequent transfer of the validated AE analysis techniques to larger laboratory specimens and finally to real structural parts.

For the modeling of AE sources, the next step comprises the in-situ generation of cracks based on fracture mechanics laws. Using such approaches, no assumptions have to be made regarding the displacement magnitudes and the source rise-times. For the latter, a thorough investigation of the

contributions from plastic deformation and viscoelastic effects is planned for the future.

Acknowledgments

We would like to thank F. Henne from Technical University Munich for providing the specimens used, M. Plöckl for carrying out part of the experimental measurements and the State of Bavaria for the funding of this applied research.

References

[1] L. Ye, T. Schuering and K. Friedrich "Matrix morphology and fibre pull-out strength of T700/PPS and T700/PET thermoplastic composites". *Journal of Materials Science*, Vol. 30, pp 4761-4769, 1995.

[2] W.H. Prosser, K.E. Jackson, S. Kellas, B.T. Smith, J. McKeon and A. Friedman "Advanced, Waveform Based Acoustic Emission Detection of Matrix Cracking". *Materials Evaluation* Vol. 53 No. 9 pp 1052-1058, 1995.

[3] S. Huguet, N. Godina, R. Gaertner, L. Salmon and D. Villard "Use of acoustic emission to identify damage modes in glass fibre reinforced polyester". *Composites Science and Technology* Vol. 62 pp 1433–1444, 2002.

[4] J.J. Scholey, P.D. Wilcox, M.R. Wisnom and M.I. Friswell "Quantitative experimental measurements of matrix cracking and delamination using acoustic emission". *Composites: Part A* Vol. 41 pp 612-623, 2010.

[5] M. Giordano, A. Calabrò, C. Esposito, A. D'Amore and L. Nicolais "An acoustic-emission characterization of the failure modes in polymer-composite materials". *Composites Science and Technology* Vol. 58 pp 1923-1928, 1998.

[6] P.D. Wilcox, C.K. Lee, J.J. Scholey, M.I. Friswell, M.R. Wisnom and B.W. Drinkwater "Progress Towards a Forward Model of the Complete Acoustic Emission Process". *Advanced Materials Research* Vols. 13-14 pp 69-76, 2006.

[7] W.H. Prosser, M.A. Hamstad, J. Gary and A. O'Gallagher "Finite Element and Plate Theory Modeling of Acoustic Emission Waveforms". *Journal of Nondestructive Evaluation* Vol. 18 No. 3 pp 83-90, 1999.

[8] M.G.R. Sause, S. Horn "Simulation of acoustic emission in planar carbon fiber reinforced plastic specimens". *Journal of Nondestructive Evaluation*, Vol. 29, No. 2, pp 123-142, 2010.

[9] M. Ohtsu and K. Ono "The generalized theory and source representation of acoustic emission". *Journal of Acoustic Emission* Vol. 5 pp 124-133, 1986.

[10] M.A. Hamstad, A. O'Gallagher and J. Gary "A wavelet transform applied to acoustic emission signals: Part 1: source identification", *Journal of Acoustic Emission* Vol. 20 pp 39-61, 2002.

[11] M.G.R. Sause and S. Horn "Simulation of Lamb Wave Excitation for Different Elastic Properties and Acoustic Emission Source Geometries". *Journal of Acoustic Emission* Vol. 28 pp 109-121, 2010.

[12] M.G.R. Sause and S. Horn "Influence of Specimen Geometry on Acoustic Emission Signals in Fiber Reinforced Composites: FEM-Simulations and Experiments". *Proceedings of 29th European Conference on Acoustic Emission Testing*, Vienna, 2010.

[13] M.G.R. Sause and S. Horn "Influence of Internal Discontinuities on Ultrasonic Signal Propagation in Carbon Fiber Reinforced Plastics". *Proceedings of 30th European Conference on Acoustic emission Testing*, Granada, 2012.

[14] M.G.R Sause M.A. Hamstad and S. Horn "Finite element modeling of conical acoustic emission sensors and corresponding experiments". *Sensors and Actuators A: Physical* Vol. 184 pp 64-71, 2012.

[15] M.J. Hinton, A.S. Kaddour and P.D. Soden *"Failure Criteria in Fibre Reinforced Polymer Composites"*. 1st edition, Elsevier Ltd., 2004.

[16] A.E. Scott, M. Mavrogordato, P. Wright, I. Sinclair and S.M. Spearing "In situ fibre fracture measurement in carbon–epoxy laminates using high resolution computed tomography". *Composites Science and Technology* Vol. 71 pp 1471-1477, 2011.

[17] A. Puck and H. Schürmann "Failure Analysis of FRP Laminates by Means of Physically Based Phenomenological Models". Composite Science and Technology Vol. 58 pp 1045–1067, 1998.

[18] M.G.R. Sause, A. Gribov, A. R. Unwin and S. Horn "Pattern recognition approach to identify natural clusters of acoustic emission signals". *Pattern Recognition Letters*, Vol. 33, No. 1, pp 17-23, 2012.

[19] M. Plöckl, M.G.R. Sause, J. Scharringhausen and S. Horn "Failure Analysis of NOL-Ring Specimens by Acoustic Emission". Proceedings of 30th European Conference on Acoustic emission Testing, Granada, 2012.

[20] M.G.R. Sause and S. Horn "Quantification of the Uncertainty of Pattern Recognition Approaches Applied to Acoustic Emission Signals" *Journal of Nondestructive Evaluation* doi:10.1007/s10921-013-0177-9, 2013.

[21] M.G.R. Sause, T. Müller, A. Horoschenkoff and S. Horn "Quantification of failure mechanisms in mode-I loading of fiber reinforced plastics utilizing acoustic emission analysis". *Composite Science and Technology*, Vol. 72, pp 167-174, 2012.